Article

Quantum simulation of conical intersections using trapped ions

Jacob Whitlow [1,2], Zhubing Jia [1,3,6], Ye Wang [1,2,7], Chao Fang [1,2], Jungsang Kim [1,2,3,4] & Kenneth R. Brown [1,2,3,5]

Conical intersections often control the reaction products of photochemical processes and occur when two electronic potential energy surfaces intersect. Theory predicts that the conical intersection will result in a geometric phase for a wavepacket on the ground potential energy surface, and although conical intersections have been observed experimentally, the geometric phase has not been directly observed in a molecular system. Here we use a trapped atomic ion system to perform a quantum simulation of a conical intersection. The ion's internal state serves as the electronic state, and the motion of the atomic nuclei is encoded into the motion of the ions. The simulated electronic potential is constructed by applying state-dependent optical forces to the ion. We experimentally observe a clear manifestation of the geometric phase using adiabatic state preparation followed by motional state measurement. Our experiment shows the advantage of combining spin and motion degrees for quantum simulation of chemical reactions.

Simulation of the quantum mechanics of molecules is an important and natural utilization of quantum simulators, with applications in calculating ground state energies and chemical reaction rates[1,2]. Classical computers have difficulty simulating the exact dynamics of even relatively simple molecules, usually resorting to an assortment of approximations to overcome the exponentially scaling Hilbert space. The Born–Oppenheimer approximation often is used to limit the size of the Hilbert space, taking advantage of the mass differences between nuclei and electrons to separate their wavefunctions. The slow-moving nuclear positions can then be treated as parameters when calculating the energy state of the fast-moving electrons. This allows one to visualize the movement of the nuclei on electronic state-dependent adiabatic potential energy surfaces parameterized by the nuclear coordinates. This approximation breaks down when the potential energy surfaces cross at a conical intersection[3,4]. Near these singularities, the couplings between the nuclear and electronic coordinates become too strong to ignore. In the vicinity of these intersections, non-trivial geometric phases come into play[5]. Such a phase depends on the direction of travel

and the solid angle encompassed by the nuclear wavefunction as it makes a loop with respect to the conical intersection. Phase interference not predicted by the energy dynamics of the system can result if different parts of the wavefunction take different paths around the intersection. Despite experimental proposals utilizing ultra-short laser pulses with stable phase differences[6,7], direct observation of geometric phase has been elusive. This is because conical intersections are difficult to probe in real systems owing to the ultra-fast and non-radiative nature of state transitions in their vicinity[8–10].

Quantum simulators do not run into the scaling problems that classical computers experience when performing chemical calculations[2,11,12]. They have already been suggested as a means of probing conical intersections and other molecular phenomena[13–19]. Early results on calculating branching ratios have been demonstrated on superconducting systems[20], and a similar phenomenon in condensed matter systems has been simulated with ultra-cold atom systems[21]. Here, we explore geometric phase interference in a system based on chains of trapped ions, which are proving to be a robust and highly controllable

[1]Duke Quantum Center, Duke University, Durham, NC, USA. [2]Department of Electrical and Computer Engineering, Duke University, Durham, NC, USA. [3]Department of Physics, Duke University, Durham, NC, USA. [4]IonQ, Inc., College Park, MD, USA. [5]Department of Chemistry, Duke University, Durham, NC, USA. [6]Present address: Department of Physics, The University of Illinois at Urbana-Champaign, Urbana, IL, USA. [7]Present address: School of Physical Sciences, University of Science and Technology of China, Hefei, China. ✉e-mail: ken.brown@duke.edu
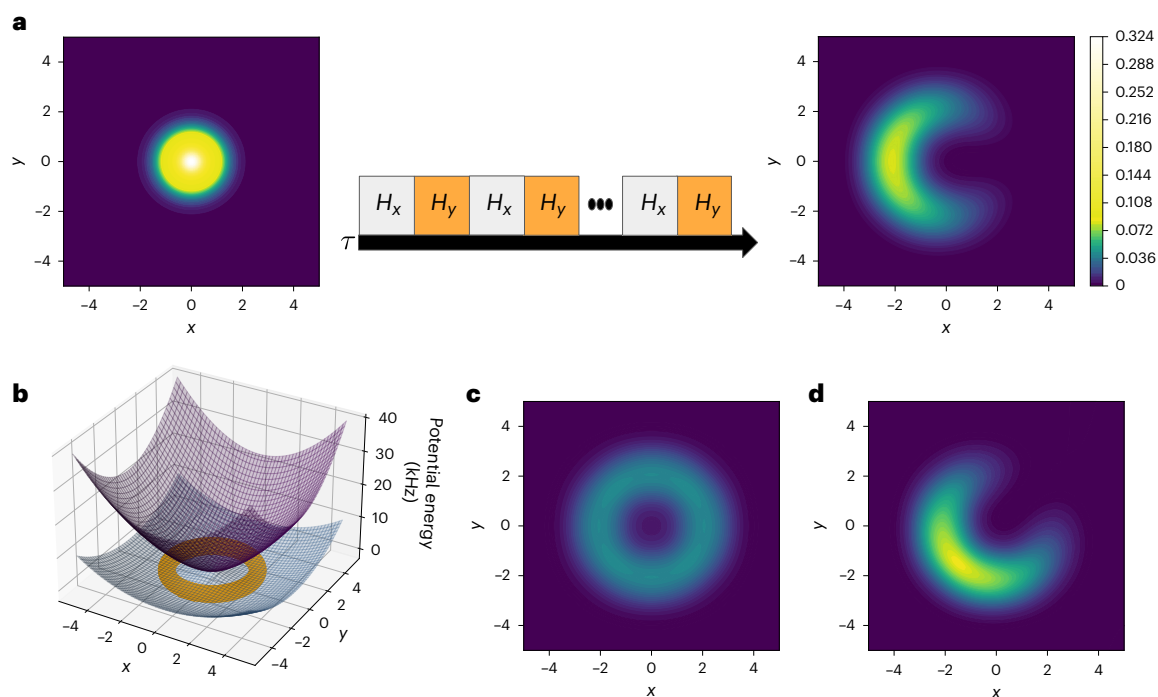
Fig. 1 | Overview of the simulated conical intersection and the effects on the wavefunction. a, An adiabatic evolution that switches x-mode ($H_x(t) = v\hat{n}_x + \frac{\Omega t}{2\tau}\hat{\sigma}_x(\hat{a}_x + \hat{a}_x^\dagger)$) coupling and y-mode ($H_y(t) = v\hat{n}_y + \frac{\Omega t}{2\tau}\hat{\sigma}_y(\hat{a}_y + \hat{a}_y^\dagger)$) coupling to produce $H(t) = H_x(t) + H_y(t)$ and a conical intersection. The plots show the spatial probability distributions of the wavefunction at the beginning and the end of the evolution, based on classical simulations. Owing to the path taken by the wavefunction around a conical intersection, there is geometric phase interference in the final result. All classical simulations were done with the open source package QuTiP[47]. **b**, The potential

energy surface produced by $H_x(\tau) + H_y(\tau)$ when setting v to 1 kHz and Ω to 3 kHz, revealing a conical intersection. The orange torus represents the spatial distribution of the ground subspace, where the wavefunction should remain throughout the adiabatic evolution. **c**, The probability distribution of the final state based on classical simulations, if there were no conical intersection and thus no geometric phase interference, allowing the wavefunction to meet with itself. **d**, The approximate effect of a $\frac{\Delta}{2}\sigma_z$ term in the Hamiltonian is a rotation proportional to $\Delta\tau$, where τ is the time of the evolution, as shown in this classical simulation. Experimentally, this term can arise from detuning in the applied laser pulses.

way of simulating other quantum mechanical systems[22–28]. Two internal states of an ion are chosen to represent a qubit, and lasers are used to coherently manipulate these states. Laser interactions that couple the qubit states to the motion of the chain are used to coherently entangle the ions with their own vibrational states. We utilize these vibrations to act as nuclear coordinates in a hybrid digital–analog approach to quantum simulation[13,29]. We use adiabatic evolution of an ion's wavefunction to provide an experimental demonstration of the creation and control of a conical intersection. The final spatial distribution of the wavefunction is measured, exhibiting interference arising from non-trivial geometric phase.

Results and discussion
Model Hamiltonian and ideal results
Initially, we consider an ideal Hamiltonian of the form

$$\hat{H}_{\text{ideal}} = \frac{v}{2}\left(p_x^2 + p_y^2 + x^2 + y^2\right) + \frac{\Omega}{\sqrt{2}}\left(\hat{\sigma}_x x + \hat{\sigma}_y y\right). \quad (1)$$

This Hamiltonian describes a spin-$\frac{1}{2}$ particle in a two-dimensional (2D) harmonic oscillator with vibrational frequency v, where the spin of the particle is coupled to its own position via the Pauli operators σ_x and σ_y with a strength Ω. The dimensionless positions, x and y, and momenta, p_x and p_y, are normalized by a factor of $\frac{1}{\sqrt{mv}}$ and $\sqrt{mv}$, respectively, where m is the particle's mass, and we set $\hbar = 1$ throughout the manuscript. The positions and momenta are first considered as

parameters for the spin Hamiltonian, as in the Born–Oppenheimer approximation. The energies of the spin eigenstates, which correspond to the electronic eigenstates, are coupled in opposite ways to the positions in the harmonic oscillators. The eigenenergies for the higher (+) and lower (−) states in this system are $E_\pm(x,y) = \frac{v}{2}\left(p_x^2 + p_y^2\right) + V_\pm(x,y)$, where $V_\pm(x,y) = \frac{v}{2}\left(x^2 + y^2\right) \pm \frac{1}{\sqrt{2}}\sqrt{\Omega^2 x^2 + \Omega^2 y^2}$ is the spin-dependent potential energy of the system. A plot of $V_\pm(x,y)$ is shown in Fig. 1b, where a conical intersection can clearly be seen.

An important feature of this semi-classical Hamiltonian is the possibility of a geometric phase that depends only on the movement through space[5,30]. This phase is entirely separate from the energy-dependent one that accumulates over time and is most prominent during an adiabatic evolution within a single eigenenergy subspace, when transitions to other subspaces can be ignored (see 'Trotter product evolution and adiabatic criteria' section in Methods). Specifically, if x and y were time-dependent parameters in this system ($x(t)$ and $y(t)$), and the system were to start in one of the eigenstates of the Hamiltonian in equation (1), we would see the following adiabatic time evolution:

$$|\psi(t)\rangle = T\exp\left(-i\int^t dt' \hat{H}(t')\right)|\psi_{n,0}\rangle$$
$$= e^{-i\int^t dt' E_n(\mathbf{R}(t'))}e^{i\gamma_n(t)}|\psi_n(\mathbf{R}(t))\rangle. \quad (2)$$

Here, T is the time ordering operator, $\mathbf{R}(t) = (x(t), y(t))$ is the position of the particle, $E_n(\mathbf{R}(t))$ is the position-dependent energy of the nth
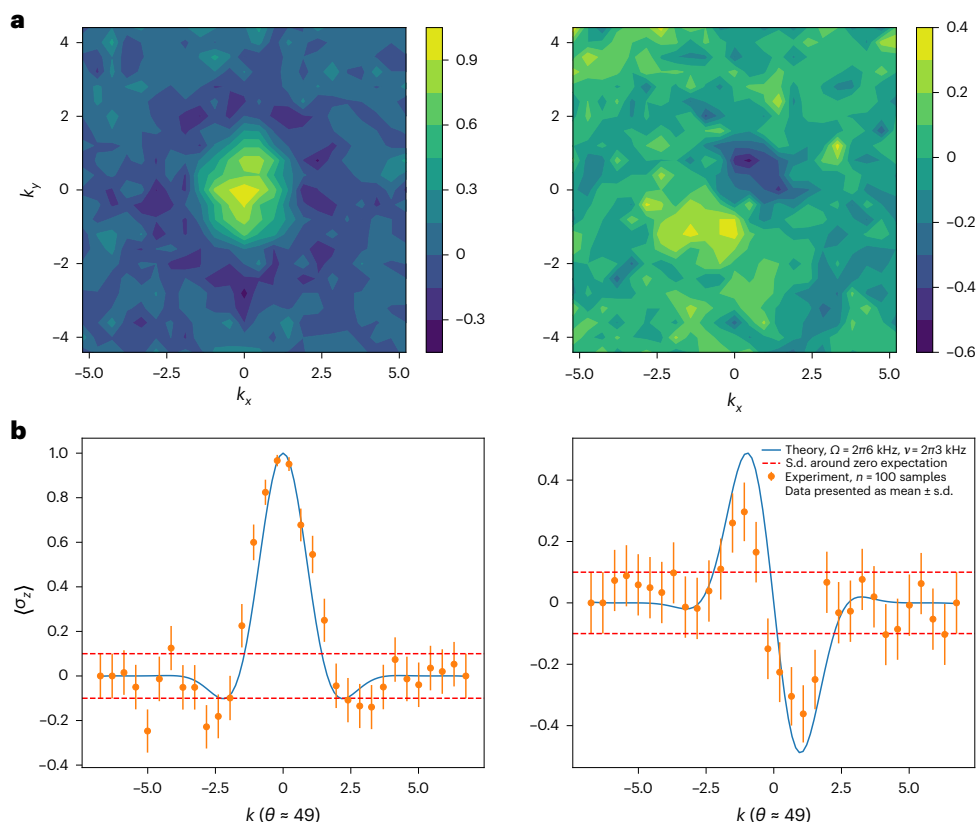
a

b

Fig. 2 | Experimental data before the Fourier transform. a, Result of Fourier push on second ion, that is, applying the unitary evolution $U(k_x, k_y) = \exp\left(-\frac{i}{2}\sigma_x(k_x\hat{x} + k_y\hat{y})\right)$ using spin-dependent laser interactions, after adiabatically evolving the first ion around the conical intersection. The second ion starts in the positive σ_z eigenstate (left) and σ_y eigenstate (right), and the plots show measured values of $\langle\sigma_z\rangle$ based on 100 experiments for each data point. Axes are the **k** vectors associated with the push, calculated based on experimental laser interaction strengths. The data are rotated by 49° compared with theory, most probably owing to an ac Stark shift caused by laser interactions during the experiment. Taking a 2D inverse Fourier transform of this data will provide the spatial distribution of the wavefunction. **b**, Cutout of experimental data along a line 49° to the horizontal, with σ_z eigenstate (left) and σ_y eigenstate (right), compared with classically simulated data with the same laser interaction parameters. Shot noise dominates our measurement uncertainty, especially when the expected value is zero (this uncertainty is indicated by the dashed orange lines), and we see good qualitative agreement up to this point. Error bars are calculated based on a binomial distribution with 100 shots per data point.

eigenstate $|\psi_n(\mathbf{R}(t))\rangle$ and $\gamma_n(t)$ is the geometric phase associated with that state, described by the equation

$$\gamma_n = i\int^t dt' \langle\psi_n(\mathbf{R}(t'))|\nabla_\mathbf{R}\psi_n(\mathbf{R}(t'))\rangle \cdot \dot{\mathbf{R}}(t') \qquad (3)$$

$$= i\int_{\mathbf{R}_0}^{\mathbf{R}_f} d\mathbf{R}' \cdot \langle\psi_n(\mathbf{R}')|\nabla_{\mathbf{R}'}\psi_n(\mathbf{R}')\rangle, \qquad (4)$$

where $\mathbf{R}_0 = \mathbf{R}(0)$ and $\mathbf{R}_f = \mathbf{R}(t)$ are initial and final positions. Given that the spin eigenstates as a function of position can be written as $|\pm(x,y)\rangle = \frac{1}{\sqrt{2}}(|0\rangle \pm \frac{x+iy}{\sqrt{x^2+y^2}}|1\rangle)$, this amounts to the integral

$$\gamma_\pm = \frac{1}{2}\int_{x_0,y_0}^{x_f,y_f} \frac{y\,dx - x\,dy}{x^2 + y^2}. \qquad (5)$$

Berry originally pointed out that, if the path taken through this position space were to perform a closed loop C around a degeneracy point, the phase would be equal to one-half of the solid angle, 2π, subtended by the loop around that point: $\gamma(C) = \pi$. Wavepackets that travel in opposite directions around the degeneracy point acquire opposing geometric phases that interfere destructively, an effect we experimentally verify in this work.

Another parameter that can be added to our system is the energy difference between the $|0\rangle$ and $|1\rangle$ spin states, Δ. This would add $\frac{\Delta}{2}\sigma_z$ to our Hamiltonian, which creates an avoided crossing in the system where the conical intersection would be. If $\Delta \ll \Omega$, this type of system is still highly non-adiabatic in behaviour and also allows for geometric phase interference based on the solid angle argument, where the solid angle is now $2\pi\left(1 - \frac{\Delta}{\sqrt{\Omega^2+\Delta^2}}\right)$ (refs. 5,30). The topological nature of this system is less obvious however, because we are missing the singularity associated with the intersection. However, by moving into the rotating spin frame, we bring back the intersection with the new Hamiltonian

$$\hat{H} = \hat{H}_{\text{H.O.}} + \frac{\Omega}{\sqrt{2}}(e^{-i\Delta t}(x - iy)\sigma_- + \text{h.c.}). \qquad (6)$$

Here, $\hat{H}_{\text{H.O.}}$ is the classical 2D harmonic oscillator, $\sigma_\pm = \frac{1}{2}(\sigma_x \mp i\sigma_y)$ and h.c. indicates the Hermitian conjugate. The potential energy surface is the same as in equation (1), but the axes are rotating. When the energy difference is small compared with the strength of the coupling, this has the effect of adiabatically moving the wavefunction around the intersection. The geometric phase remains present in the system, despite this unitary transformation, as does the topological nature of the system.
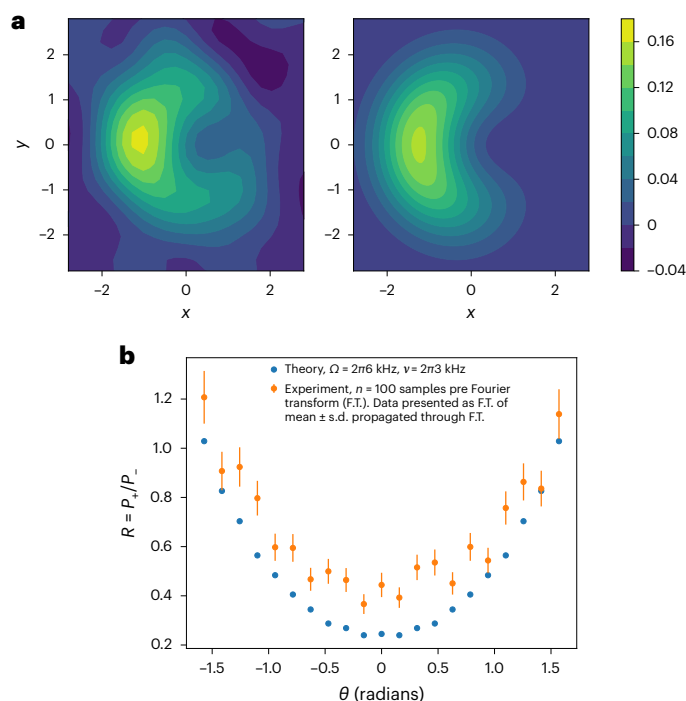
Fig. 3 | Experimental data after the Fourier transform. a, Experimental results (left) and classical simulation results (right) after adiabatic evolution of ion chain's wavefunction around a conical intersection in normal coordinate space, defined by $\hat{H}(t) = \hat{H}_x(t) + \hat{H}_y(t)$ from Fig. 1, where $v = 2\pi \times 3$ kHz, $\Omega = 2\pi \times 6$ kHz and total evolution time $\tau = 330$ μs. The experimental data are the inverse Fourier transform of the raw experimental data in Fig. 2 rotated by 49° due to ac Stark shift compensation. In theory, this should be a pure probability distribution, as is the case for the classical simulation results, but experimental error and measurement statistics allow for negative values. The experimental data show a clear sign of phase interference on the opposite site of the conical intersection, in agreement with the results produced by classical simulation. **b,** This plot shows the integral of one-half of the distribution divided by the integral of the other half, where the line defining the halfway point is rotated by the angle θ. The dip in the experimental results and the qualitative agreement with the classical simulation indicate the presence of geometric phase interference. Error bars are calculated based on propagation of error through the inverse Fourier transform, then a Taylor expansion when taking the ratios.

A more accurate model requires coupling between the nuclear and electronic quantum states because of the proximity to the intersection and breakdown of the Born–Oppenheimer approximation. Assuming vanishing Δ, this leads to the following fully quantum Hamiltonian

$$\hat{H}_{ideal} = v\hat{n}_x + v\hat{n}_y + \frac{\Omega}{2}\hat{\sigma}_x(\hat{a}_x + \hat{a}_x^\dagger) + \frac{\Omega}{2}\hat{\sigma}_y(\hat{a}_y + \hat{a}_y^\dagger). \qquad (7)$$

Here, we have replaced position ξ and momentum p_ξ by ladder operators $\frac{1}{\sqrt{2}}(\hat{a}_\xi + \hat{a}_\xi^\dagger)$ and $\frac{-i}{\sqrt{2}}(\hat{a}_\xi - \hat{a}_\xi^\dagger)$, respectively, where $\xi \in \{x, y\}$. This Hamiltonian is associated with the Jahn–Teller effect, or Rashba coupling if position is replaced by momentum in the spin–motion coupling, as is common in condensed matter physics[31–33]. The subspace of degenerate ground states for this Hamiltonian forms a ring around the origin as one would expect from the energy surfaces plotted in Fig. 1b. Importantly, the arguments for geometric phase still apply in this fully quantized picture, just with a larger Hilbert space.

The essence of our experiment is as follows: Start with a qubit in the eigenstate of σ_x, $|+\rangle$, and in the ground state of a 2D harmonic oscillator. Then, adiabatically turn on coupling to the motional modes of

the harmonic oscillator in such a way that the path taken by the wavefunction splits up and meets on the other side. Ideally, we turn on both the motional couplings at once, as described by

$$\hat{H}(t) = v\hat{n}_x + v\hat{n}_y + \frac{\Omega t}{2\tau}\hat{\sigma}_x(\hat{a}_x + \hat{a}_x^\dagger) + \frac{\Omega t}{2\tau}\hat{\sigma}_y(\hat{a}_y + \hat{a}_y^\dagger). \qquad (8)$$

Here τ is the time of the evolution. The equations of motion based on the dynamics of the Hamiltonian are

$$\langle\ddot{x}\rangle = -v^2\langle x\rangle - \frac{\Omega v t}{\sqrt{2}\tau}\langle\sigma_x\rangle,$$
$$\langle\ddot{y}\rangle = -v^2\langle y\rangle - \frac{\Omega v t}{\sqrt{2}\tau}\langle\sigma_y\rangle. \qquad (9)$$

Owing to the symmetry breaking of starting in the $|+\rangle$ state, $\langle\sigma_x\rangle$ dominates for small t (Supplementary Note 4). There is thus an initial push in the negative x direction, followed by a path that encircles the intersection. Experimentally, we performed the evolution by breaking the coupling to the x mode and y mode into separate steps in time and treating the overall unitary as a Trotter product (see 'Trotter product evolution and adiabatic criteria' section in Methods). This discretization allows for a digital approach to our simulation where we can calibrate for each pulse type as opposed to calibrating for the whole evolution. This procedure is shown in Fig. 1a, along with classically simulated data. The final ideal state of the trajectory is a crescent shape owing to interference on the other side of the conical intersection. Importantly, this interference must be a result of geometric phase because the system will remain in the ground state throughout the adiabatic evolution, leading to no energy-dependent phase difference. This attribution is confirmed by Fig. 1c, where a Hamiltonian with only the bottom portion of the potential energy is used to simulate the evolution, resulting in a ring. In Fig. 1d, we show the results if $\frac{\Delta}{2}\sigma_z$ were included, where $\Delta \ll \Omega$, v. The wavefunction is rotated slightly as predicted by moving into the rotating frame in equation (6).

Experimental results

We performed the experiment on a room temperature system designed to trap ^{171}Yb$^+$ ions[34,35]. To have access to higher order normal modes that are less susceptible to electric field noise and heating rates[36], we optimized the system to address the centre ion of a five-ion string. The atomic states and the motional modes are manipulated with laser-based interactions to mimic the desired Hamiltonian (see 'Experimental setup and trapped ion Hamiltonian' section in Methods). The normal coordinate distribution was measured using a 'Fourier push' method[37,38]. By using a second ion that couples into the same modes that we used for the simulation, we can perform two separate spin-dependent pushes to create the unitary evolution $U(k_x, k_y) = \exp\left(-\frac{i}{2}\sigma_x(k_x\hat{x} + k_y\hat{y})\right)$. We then extract the characteristic function or the Fourier transform of the spatial distribution by measuring the expectation of the Pauli operator σ_z for this ion (see 'Measurement procedure' section in Methods). The even (odd) information is obtained by starting the second ion in the positive σ_z (σ_y) eigenstate. The results of these measurements are shown in Fig. 2a. The results have been rotated by about 49° owing to a detuning from the resonant transition, most probably caused by ac Stark shifts, adding an effective energy difference in the spin states. In Fig. 2b, we see a cutout of this data along the 49° line, where the most prominent features are present, in comparison with classical simulation. After $k \approx 3.3$, the data evens out at about zero, which corresponds to the point of highest shot noise when making measurements. We cut off at this point when taking the inverse Fourier transform to avoid high-frequency features due to the shot noise.

The result of taking the inverse Fourier transform of the measured data is shown in Fig. 3a, where a clear crescent shape emerges after the adiabatic evolution. We rotated the axes by the necessary 49° to match

the high-density region with the ideal evolution. This is effectively a post-measurement ac Stark shift compensation. In this experiment, we chose $\nu = 2\pi \times 3$ kHz and $\Omega = 2\pi \times 6$ kHz, and we determine our Stark shift to be around $\Delta = 2\pi \times 0.8$ kHz on the basis of simulations. These numbers were subject to drift of about 10% over the course of the day, resulting in some experimental uncertainty. We chose an experimental time of 330 μs, which does not satisfy the criteria for adiabaticity for a linear ramp based only on energy level spacing. However, owing to symmetries in the system, some transitions are forbidden and the effective splitting between states is higher (see 'Trotter product evolution and adiabatic criteria' section in Methods). Still, because our experiment only approximately met the adiabatic condition, there were slight oscillations due to non-adiabatic transitions. The time of 330 μs is also perfectly timed with the most outward point of the initial oscillation (that is, $\frac{2\pi}{\nu}$), making the crescent-shaped wavefunction the most visible. Note that no post-processing of the data was done other than normalization of the distribution. The results should be a probability distribution in theory, but negative quantities appear in the far corners due to measurement statistics and experimental error from drift over the course of the experiment.

The measured distribution exhibits all the sought-after qualitative features, specifically regions of maximum and minimum density on a ring-like shape. We also compare it with the ideal results using the ratio of the distribution on one-half of the plot versus that on the other, adjusting the angle θ of the line that defines the halfway point. This is described mathematically by

$$R(\theta) = \frac{\int_{+,\theta} dx\, dy\, P(x,y)}{\int_{-,\theta} dx\, dy\, P(x,y)}. \tag{10}$$

Here, $P(x,y)$ is the spatial distribution of the wavepacket. The θ indicates the angle of the dividing line, with $\theta = 0$ corresponding to a vertical line, and the '+' and '−' signs indicate whether the integral was taken on the positive or negative side of that line. Ideally, almost all of the distribution is on one side of the plot for $\theta = 0$, and this ratio goes to one as θ approaches $\pm\frac{\pi}{2}$. Experimentally, we see this general pattern but shifted up owing to experimental noise. This noise can come from many things, including non-adiabatic dynamics, off-resonant coupling into other modes, motional phase mismatch, frequency drifts in our motional modes, our system not starting in the harmonic oscillator ground state, our system heating over time and system preparation and measurement error. The qualitative agreement shows the robustness of this effect to noise.

Conclusion

We provide experimental evidence for geometric phase interference in simulated conical intersections in trapped ions. We utilize spin-dependent laser pushes to create an adiabatic potential energy surface that mimics that of a small molecule. We adiabatically evolve the ion chain under the Hamiltonian, then measure interference in the spatial distribution owing to the accumulated geometric phase. These findings should advance work on quantum simulation of chemical systems with trapped ions to include systems with strong nuclear–electronic interactions.

The next step is to utilize conical intersections to work towards quantum advantage for a practical problem in quantum chemistry. One can imagine a system that utilizes multiple ions to create more complicated potential energy surfaces with more than one crossing between more than two levels. There are also many more motional modes available in large ion chains, meaning we can create high-dimensional potential energy surfaces with multiple crossings, quickly escalating the necessary Hilbert space while maintaining simulability on trapped ion systems. Work has also been done to utilize the second-order sidebands in trapped ion systems for entangling gates[39,40]. Such operations increase the complexity of the potential energy surfaces available by adding quadratic terms. We can also utilize the bosonic modes as bath modes in an open quantum system[13,25,41], allowing us to take advantage of decoherence as a tool that mimics noise in the environment.

There are also tools from digital quantum simulation that can be utilized in analog simulations. Frequency- and amplitude-modulated pulses can be used to couple into specific modes while decoupling from others, overcoming the problem of mode crowding and off-resonant coupling[42,43]. Fermionic degrees of freedom can be brought in via the Jordan–Wigner or Bravyi–Kitaev transformations, well-established techniques that map Pauli operators to Fermionic ones[44,45]. We can use the Trotter product formula to combine these modulation techniques and Fermionic mappings with the non-adiabatic bosonic models simulated in this paper to create molecular Hamiltonians of arbitrary size and complexity, if the number of ions and the coherence times allow for it. This hybrid digital–analog approach can scale in a polynomial way with the number of degrees of freedom that we wish to simulate[2,13], opening up the path to practical quantum advantage for scientific computation.

We have recently become aware of work done by the University of Sydney on a similar experiment with a single trapped ion quantum simulator[46]. Their experiment explores the effects of geometric phase on the dynamics of a wavefunction as it travels around an engineered conical intersection. This complements our own experiment as it demonstrates how the time-dependent behaviour of a system not in an eigenstate of the Hamiltonian can be affected by geometric phase in non-trivial ways.

Online content

Any methods, additional references, Nature Portfolio reporting summaries, source data, extended data, supplementary information, acknowledgements, peer review information; details of author contributions and competing interests; and statements of data and code availability are available at https://doi.org/10.1038/s41557-023-01303-0.

References

1. McArdle, S., Endo, S., Aspuru-Guzik, A., Benjamin, S. C. & Yuan, X. Quantum computational chemistry. *Rev. Mod. Phys.* **92**, 015003 (2020).
2. Kassal, I., Jordan, S. P., Love, P. J., Mohseni, M. & Aspuru-Guzik, A. Polynomial-time quantum algorithm for the simulation of chemical dynamics. *Proc. Natl Acad. Sci. USA* **105**, 18681–18686 (2008).
3. Larson, J., Sjöqvist, E. & Öhberg, P. *Conical Intersections in Physics* (Springer, 2020).
4. Yarkony, D. R. Diabolical conical intersections. *Rev. Mod. Phys.* **68**, 985 (1996).
5. Berry, M. V. Quantal phase factors accompanying adiabatic changes. *Proc. R. Soc. Lond. A.* **392**, 45–57 (1984).
6. Cina, J. A., Smith Jr, T. J. & Romero-Rochín, V. Time-resolved optical tests for electronic geometric phase development. *Adv. Chem. Phys.* **83**, 1–42 (1992).
7. Cina, J. A. Phase-controlled optical pulses and the adiabatic electronic sign change. *Phys. Rev. Lett.* **66**, 1146 (1991).
8. Farag, M. H., Jansen, T. L. & Knoester, J. Probing the interstate coupling near a conical intersection by optical spectroscopy. *J. Phys. Chem. Lett.* **7**, 3328–3334 (2016).
9. Köppel, H. Ultrafast non-radiative decay via conical intersections of molecular potential-energy surfaces: $C_2H_4^+$. *Chem. Phys.* **77**, 359–375 (1983).
10. Chen, L., Gelin, M. F., Zhao, Y. & Domcke, W. Mapping of wave packet dynamics at conical intersections by time-and frequency-resolved fluorescence spectroscopy: a computational study. *J. Phys. Chem. Lett.* **10**, 5873–5880 (2019).
11. Blatt, R. & Roos, C. F. Quantum simulations with trapped ions. *Nat. Phys.* **8**, 277–284 (2012).

12. Lloyd, S. Universal quantum simulators. *Science* **273**, 1073–1078 (1996).

13. MacDonell, R. J. et al. Analog quantum simulation of chemical dynamics. *Chem. Sci.* **12**, 9794–9805 (2021).

14. Gambetta, F. M., Zhang, C., Hennrich, M., Lesanovsky, I. & Li, W. Exploring the many-body dynamics near a conical intersection with trapped rydberg ions. *Phys. Rev. Lett.* **126**, 233404 (2021).

15. Wüster, S., Eisfeld, A. & Rost, J. Conical intersections in an ultracold gas. *Phys. Rev. Lett.* **106**, 153002 (2011).

16. Wüster, S. & Rost, J. M. Rydberg aggregates. *J. Phys. B.* **51**, 032001 (2018).

17. MacDonell, R. J. et al. Predicting molecular vibronic spectra using time-domain analog quantum simulation. Preprint at *arXiv* https://doi.org/10.48550/arXiv.2209.06558 (2022).

18. Omiya, K. et al. Analytical energy gradient for state-averaged orbital-optimized variational quantum eigensolvers and its application to a photochemical reaction. *J. Chem. Theory Comput.* **18**, 741–748 (2022).

19. Tamiya, S., Koh, S. & Nakagawa, Y. O. Calculating nonadiabatic couplings and berry's phase by variational quantum eigensolvers. *Phys. Rev. Res.* **3**, 023244 (2021).

20. Wang, C. S. et al. Observation of wave-packet branching through an engineered conical intersection. *Phys. Rev. X* **13**, 011008 (2023).

21. Brown, C. D. et al. Direct geometric probe of singularities in band structure. *Science* **377**, 1319–1322 (2022).

22. Nam, Y. et al. Ground-state energy estimation of the water molecule on a trapped-ion quantum computer. *npj Quantum Inf.* **6**, 1–6 (2020).

23. Hempel, C. et al. Quantum chemistry calculations on a trapped-ion quantum simulator. *Phys. Rev. X* **8**, 031022 (2018).

24. Porras, D., Ivanov, P. A. & Schmidt-Kaler, F. Quantum simulation of the cooperative Jahn–Teller transition in 1D ion crystals. *Phys. Rev. Lett.* **108**, 235701 (2012).

25. Gorman, D. J. et al. Engineering vibrationally assisted energy transfer in a trapped-ion quantum simulator. *Phys. Rev. X* **8**, 011038 (2018).

26. Richerme, P. et al. Quantum computation of hydrogen bond dynamics and vibrational spectra. Preprint at *arXiv* https://doi.org/10.48550/arXiv.2204.08571 (2022).

27. Monroe, C. et al. Programmable quantum simulations of spin systems with trapped ions. *Rev. Mod. Phys.* **93**, 025001 (2021).

28. Nguyen, N. H. et al. Digital quantum simulation of the Schwinger model and symmetry protection with trapped ions. *PRX Quantum* **3**, 020324 (2022).

29. Georgescu, I. M., Ashhab, S. & Nori, F. Quantum simulation. *Rev. Mod. Phys.* **86**, 153 (2014).

30. Berry, M. et al. Anticipations of the geometric phase. *Phys. Today* **43**, 34–40 (1990).

31. Longuet-Higgins, H. C., Öpik, U., Pryce, M. H. L. & Sack, R. Studies of the Jahn–Teller effect. II. The dynamical problem. *Proc. R. Soc. Lond. A* **244**, 1–16 (1958).

32. Manchon, A., Koo, H. C., Nitta, J., Frolov, S. & Duine, R. New perspectives for Rashba spin–orbit coupling. *Nat. Mater.* **14**, 871–882 (2015).

33. Lin, Y.-J., Jiménez-García, K. & Spielman, I. B. Spin–orbit-coupled Bose–Einstein condensates. *Nature* **471**, 83–86 (2011).

34. Wang, Y. et al. High-fidelity two-qubit gates using a microelectromechanical-system-based beam steering system for individual qubit addressing. *Phys. Rev. Lett.* **125**, 150505 (2020).

35. Jia, Z. et al. Determination of multimode motional quantum states in a trapped ion system. *Phys. Rev. Lett.* **129**, 103602 (2022).

36. Wineland, D. J. et al. Experimental issues in coherent quantum-state manipulation of trapped atomic ions. *J. Res. Natl. Inst. Stand. Technol.* **103**, 259 (1998).

37. Gerritsma, R. et al. Quantum simulation of the dirac equation. *Nature* **463**, 68–71 (2010).

38. Flühmann, C. & Home, J. P. Direct characteristic-function tomography of quantum states of the trapped-ion motional oscillator. *Phys. Rev. Lett.* **125**, 043602 (2020).

39. Katz, O. & Monroe, C. Programmable quantum simulations of bosonic systems with trapped ions. *Phys. Rev. Lett.* **131**, 033604 (2023).

40. Katz, O., Cetina, M. & Monroe, C. Programmable N-body interactions with trapped ions. Preprint at *arXiv* https://doi.org/10.48550/arXiv.2207.10550 (2022).

41. Lemmer, A. et al. A trapped-ion simulator for spin-boson models with structured environments. *New J. Phys.* **20**, 073002 (2018).

42. Roos, C. F. Ion trap quantum gates with amplitude-modulated laser beams. *New J. Phys.* **10**, 013002 (2008).

43. Leung, P. H. et al. Robust 2-qubit gates in a linear ion crystal using a frequency-modulated driving force. *Phys. Rev. Lett.* **120**, 020501 (2018).

44. Batista, C. & Ortiz, G. Generalized Jordan–Wigner transformations. *Phys. Rev. Lett.* **86**, 1082 (2001).

45. Seeley, J. T., Richard, M. J. & Love, P. J. The Bravyi–Kitaev transformation for quantum computation of electronic structure. *J. Chem. Phys.* **137**, 224109 (2012).

46. Valahu, C. H. et al. Direct observation of geometric phase in dynamics around a conical intersection. Preprint at *arXiv* https://doi.org/10.48550/arXiv.2211.07320 (2022).

47. Johansson, J. R., Nation, P. D. & Nori, F. QuTiP: an open-source python framework for the dynamics of open quantum systems. *Comput. Phys. Commun.* **183**, 1760–1772 (2012).

Methods

Experimental setup and trapped ion Hamiltonian

The system utilizes the hyperfine states of the centre ion as its qubits, that is, $|F = 0, m_F = 0\rangle = |0\rangle$ and $|F = 1, m_F = 0\rangle = |1\rangle$ of the $^2S_{1/2}$ manifold, split by $(2\pi)12.6428$ GHz[48]. The ions sit in a pseudo-harmonic potential on a micro-fabricated linear Paul trap that can be modelled as a quantum harmonic oscillator[49]. We use 370 nm light, resonant with the $^2S_{1/2} \rightarrow {}^2P_{1/2}$ transition, to perform Doppler cooling, detection and initialization.

Transitions between qubit state are made via Raman transition with two tones of a pulsed 355 nm laser[50,51]. Such transitions can be coupled to the motion of the ion by detuning one of the laser tones from the resonant transition frequency by the frequency of the harmonic motion of the ion. The detuning can be negative or positive, referred to as red or blue sideband transitions, respectively. The effective Hamiltonians in the interaction frame for each tone can be written as

$$\hat{H}_{\text{red}} = v\hat{n} + \frac{\Omega}{2}(\sigma_+ a e^{-i\phi} + \sigma_- a^\dagger e^{i\phi}),$$
$$\hat{H}_{\text{blue}} = v\hat{n} + \frac{\Omega}{2}(\sigma_- a e^{-i\phi} + \sigma_+ a^\dagger e^{i\phi}). \tag{11}$$

The parameters v, Ω and ϕ are the detuning from the motional transition, the Rabi frequency and the phase of the laser, respectively. Note that both the atomic transition coupling and the motional coupling have been incorporated into Ω (Supplementary Note 1). One can completely recreate equation (7) in the interaction picture of the system by utilizing many tones on the same acousto-optic modulators (AOMs) that couple into two modes.

Because we trap five ions in this experiment, we are no longer dealing with a distribution over real space but instead over normal-mode coordinates. The theoretical distribution is the same, and multi-ion normal modes other than the centre-of-mass mode are less susceptible to uniform electric field noise[36]. However, this has the negative effect of adding unwanted coupling into other modes (Supplementary Note 2). In our five-ion chain, we use the third highest frequency mode and the lowest frequency mode (also called the zig-zag mode), as shown in Supplementary Fig. 2c. Notably, the centre ion does not couple into the nearest-neighbour modes, reducing noise during the simulation

Trotter product evolution and adiabatic criteria

We calibrate our system to couple to one mode at a time by applying up to two simultaneous tones to our AOMs. We break the evolution of the system under the Hamiltonian into N steps, and each step into two parts given by the following equation for the Trotter product:

$$e^{-it\hat{H}} = e^{-it_x\hat{H}_x}e^{-it_y\hat{H}_y} + \mathcal{O}(t^2), \tag{12}$$

where ideally $t\hat{H} = t_x\hat{H}_x + t_y\hat{H}_y$. With the experimental sequence broken up in this way, we can calibrate for each pulse type as opposed to calibrating for the whole evolution, at the cost of error from non-commuting terms. By making t small enough for each evolution, we can remove most of this error. In our experiment, we broke up the Hamiltonian in the following way:

$$\hat{H}_{x,j} = v_x\hat{n}_x + \frac{\Omega_x j}{2N}\sigma_x(\hat{a}_x + \hat{a}_x^\dagger),$$
$$\hat{H}_{y,j} = v_y\hat{n}_y + \frac{\Omega_y j}{2N}\sigma_y(\hat{a}_y + \hat{a}_y^\dagger). \tag{13}$$

This describes the Hamiltonian at the jth of N steps, where laser power is kept constant during each step. The harmonic oscillator term $v\hat{n}$ can be simulated with a calibrated laser detuning or by adding phase proportional to the time of the interaction to the laser pulses at each step. We chose the latter because we found it easier to control at the cost of a temporal digitization of the oscillator term. This effectively breaks the evolution into four steps, with the oscillator term and the spin-dependent push treated separately. In our system, $\Omega_x \approx 2\pi \times 7.5$ kHz and $\Omega_y \approx 2\pi \times 5$ kHz owing to different motional couplings. We applied the x-mode pulse for 40% of the total step time and the y-mode pulse for 60%, leading to an effective Ω for both pulses of about $2\pi \times 6$ kHz. We broke the evolution into $N = 16$ steps, with adiabatically increasing laser strengths. This was found to incur a negligible error, based on classical simulations.

To minimize the error from decoherence, we also wished to shorten our experiment as much as possible while maintaining the following adiabatic condition for all times t (ref. 3):

$$\left| \frac{\langle\psi(t)_n| \frac{d}{dt}\hat{H}(t) |\psi(t)_m\rangle}{\Delta_{nm}^2(t)} \right| \ll 1, \tag{14}$$

where $|\psi_n(t)\rangle$ and $|\psi_m(t)\rangle$ are states in the nth and mth eigensubspaces at time t, respectively, and Δ_{nm} is the difference in energy between these two subspaces. Often overlooked in this equation is that $\frac{d}{dt}H(t)$ needs to couple the two subspaces. For our chosen experimental time of 330 μs, the difference in frequency does not actually qualify for a simple energy argument for adiabaticity. Owing to symmetries, however, the lowest subspaces are not coupled together, and this condition is met to a good approximation. In fact, simulations show that the value on the left side of inequality of equation (14) never goes above 0.3 for the first eight excited states, and is consistently below 0.2.

Measurement procedure

To confirm the success of our experiment, we need to measure the spatial distribution of the ion's wavefunction. To do this, we expand the one-dimensional (1D) 'Fourier push' applied in refs. 37,38 to get the 2D characteristic function of the spatial distribution. We take advantage of the fact that we have multiple ions in our setup, many of which are unused during the experiment and therefore their internal states are not entangled with the motion. We choose one of the experimental ion's nearest neighbours, which also couples into the modes used for simulation, and perform a state-dependent push on it, defined by

$$U(t_x, t_y) = e^{-\frac{i}{2}\sigma_x\left(\Omega_x t_x(\hat{a}_x + \hat{a}_x^\dagger) + \Omega_y t_y(\hat{a}_y + \hat{a}_y^\dagger)\right)}. \tag{15}$$

Note that the ion is pushed in the two different spatial directions for different amounts of time, t_x and t_y. This is easy enough to accomplish because pushes in different directions commute with each other, so they can be performed one after another without error. This can be recast as

$$U(k_x, k_y) = e^{-\frac{i}{2}\sigma_x(k_x x + k_y y)}. \tag{16}$$

Some simple algebra tells us that measuring the state of this ion in the σ_z basis provides the following averages:

$$\langle U(k_x, k_y)^\dagger \sigma_z U(k_x, k_y)\rangle = \langle\sigma_z \cos(k_x x + k_y y)\rangle$$
$$+ \langle\sigma_y \sin(k_x x + k_y y)\rangle. \tag{17}$$

Therefore, by performing the same experiment twice but preparing the extra ion in the positive eigenstate of the σ_z operator first and the σ_y operator second, we can construct the Fourier transform of the spatial distribution, also known as the characteristic function. Experimentally, we calculated our Rabi frequencies Ω_x and Ω_y for our second ion to be $2\pi \times 5.3$ kHz and $2\pi \times 3$ kHz, respectively. To obtain Fig. 3a, we pushed for up to 110 μs on our x mode and 165 μs on our y mode, creating a 23×23 point grid. We used phase control on our lasers to push in the negative direction for each mode.

Data availability

Source data are provided with this paper.

References

48. Olmschenk, S. et al. Manipulation and detection of a trapped yb+ hyperfine qubit. *Phys. Rev. A* **76**, 052314 (2007).
49. Revelle, M. C. Phoenix and peregrine ion traps. Preprint at *arXiv* https://doi.org/10.48550/arXiv.2009.02398 (2020).
50. Debnath, S. *A Programmable Five Qubit Quantum Computer Using Trapped Atomic Ions*. Ph.D. thesis, University of Maryland, College Park (2016).
51. Hayes, D. et al. Entanglement of atomic qubits using an optical frequency comb. *Phys. Rev. Lett.* **104**, 140501 (2010).

Author contributions

J.W. performed classical simulations, designed and ran the experiment, and wrote the paper. Z.J. performed classical simulations and designed the experiment. Y.W. and C.F. built and maintained the experimental setup. J.K. supervised the experimental setup. K.R.B. developed the original project idea and supervised the research.

Competing interests

K.R.B. is a scientific advisor for IonQ, Inc. and has a personal financial interest in the company. The remaining authors declare no competing interests.

Additional information

Supplementary information The online version contains supplementary material available at https://doi.org/10.1038/s41557-023-01303-0.

Correspondence and requests for materials should be addressed to Kenneth R. Brown.

Peer review information *Nature Chemistry* thanks Tsveta Miteva and the other, anonymous, reviewer(s) for their contribution to the peer review of this work.

Reprints and permissions information is available at www.nature.com/reprints.